



# Self-Closing of Cracks Generated in Microstructure-Controlled 400 $\mu\text{m}$ -Thick Composite Cathodes for All-Solid-State Batteries: Observed by *In Situ* Scanning Electron Microscopy with Energy-Dispersive X-Ray Spectroscopy

Kenta Watanabe,\* Han-Seul Kim, Kazuhiro Hikima, Naoki Matsui, Kota Suzuki, Hiroyuki Muto, Atsunori Matsuda, Ryoji Kanno, and Masaaki Hirayama\*

All-solid-state batteries (ASSBs) are a promising next-generation secondary battery technology. To achieve high energy and power densities, the thickness of composite electrodes must be increased. The microstructure and mechanical properties of the composites must be carefully controlled to ensure sufficient contact between particles. The 400  $\mu\text{m}$ -thick  $\text{LiCoO}_2\text{-Li}_{10.35}\text{Ge}_{1.35}\text{P}_{1.65}\text{S}_{12}$  (LCO-LGPS) composites are fabricated using LGPS with various particle sizes. The composites using small-sized LGPS particles exhibited higher capacity and retention than those using large-sized particles. *In situ* cross-sectional scanning electron microscopy with

energy-dispersive X-ray spectroscopy reveals that the cracks generated during charging demonstrated self-closing during discharge in the composite with small-sized LGPS regardless of the generated locations, leading to high-capacity retention. However, this self-closing is not observed in the composite using large-sized LGPS. The self-closing behavior depends on the microstructure and mechanical properties of ASSBs. Furthermore, this self-closing finding provides new strategies for designing the microstructure and mechanical properties of ASSBs.

## 1. Introduction

Secondary batteries have been extensively studied with a focus on enhancing energy and power densities to address the intermittent supply of electrical power derived from renewable energy sources, such as sunlight, wind, and rain. Secondary batteries are being considered as power sources for large equipment that requires large amounts of energy and power. Electric vehicles have successfully implemented Li-ion batteries (LIBs), which are the most common secondary battery type. However, to enhance the practicality of electric vehicles, it is essential to extend their cruising range, as charging LIBs requires considerably more time than refueling with gasoline. Thus, improving energy and power densities is a critical factor in the development of secondary batteries.

All-solid-state batteries (ASSBs) are promising secondary batteries with the theoretical potential to achieve high energy and power densities. Unlike traditional batteries that use liquid electrolytes, ASSBs utilize ionic conductors as solid electrolytes. This eliminates the risk of liquid electrolyte leakage, making ASSBs safer and more reliable. Consequently, ASSBs can be easily stacked without requiring individual electrolyzers (bipolar stacking), allowing for integration into a single electrolyzer.<sup>[1]</sup> This design reduces the overall volume and weight of the battery, even when using the same amount of electrode material as LIBs, resulting in an increase in energy and power densities.

To maximize the energy and power densities of ASSBs, it is essential to incorporate as much electrode active material as possible into the cathodes and anodes. However, effectively utilizing

K. Watanabe, M. Hirayama  
Department of Chemical Science and Engineering  
School of Materials and Chemical Technology  
Institute of Science Tokyo  
4259 Nagatsuta-cho, Midori-ku, Yokohama 226-8501, Japan  
E-mail: watanabe.k.c173@m.isct.ac.jp  
hirayama@mct.isct.ac.jp

H.-S. Kim  
Department of Chemical Science and Engineering  
School of Materials and Chemical Technology  
Tokyo Institute of Technology  
4259 Nagatsuta-cho, Midori-ku, Yokohama 226-8501, Japan

K. Hikima, H. Muto, A. Matsuda  
Department of Electrical and Electronic Information Engineering  
Toyohashi University of Technology  
1-1 Hibarigaoka, Tempaku-cho, Toyohashi 441-8580, Japan

N. Matsui, K. Suzuki, R. Kanno, M. Hirayama  
Research Center for All-Solid-State Battery  
Institute of Integrated Research  
Institute of Science Tokyo  
4259 Nagatsuta-cho, Midori-ku, Yokohama 226-8501, Japan

H. Muto  
Institute of Liberal Arts and Sciences  
Toyohashi University of Technology  
1-1 Hibarigaoka, Tempaku-cho, Toyohashi 441-8580, Japan

Supporting information for this article is available on the WWW under <https://doi.org/10.1002/batt.202500119>

© 2025 The Author(s). *Batteries & Supercaps* published by Wiley-VCH GmbH. This is an open access article under the terms of the Creative Commons Attribution-NonCommercial-NoDerivs License, which permits use and distribution in any medium, provided the original work is properly cited, the use is non-commercial and no modifications or adaptations are made.

these loaded active materials becomes challenging with the thickening of the electrode layers. Unlike liquid electrolytes, solid electrolytes cannot penetrate the voids between the particles of the active materials, leading to a reduced reaction area between the active materials and solid electrolytes. Composites comprising solid electrolytes and active materials are often used to ensure sufficient reaction areas. However, these composite electrodes can still contain voids, and some particle surfaces may remain uncontacted. This lack of contact complicates the formation of effective conduction pathways for electrons and ions, particularly as the thickness of the electrode layers increases. Consequently, it becomes challenging to create thick composite electrodes that fully utilize the active materials. To construct thick composite electrodes, it is essential to control the physical structures at scales ranging from several tens of nanometers to micrometers, to ensure that the contact between particles is sufficient to facilitate the necessary reactions. The physical structures at these small scales are referred to as microstructures.<sup>[2–12]</sup> Microstructures can be optimized by adjusting the size and distribution of particles within the composites, as they are influenced by the uniformity and dispersibility of the solid electrolytes and active materials. We have previously reported that the charge–discharge properties of LiCoO<sub>2</sub>–Li<sub>10</sub>GeP<sub>2</sub>S<sub>12</sub> can be improved through microstructural control using miniaturized Li<sub>10</sub>GeP<sub>2</sub>S<sub>12</sub> particles. This approach increases the number of LCO/Li<sub>10</sub>GeP<sub>2</sub>S<sub>12</sub> interfaces, which serve as reaction sites, and creates 3D ionic/electronic conduction pathways.<sup>[11]</sup> Additionally, LGPS solid electrolytes milled with ZrO<sub>2</sub> balls in wet condition (wet-milled LGPS: WM-LGPS) can effectively suppress cracking (contact loss) in the solid electrolyte layer. This improvement enhances the stability during charge–discharge cycles in Li–In|LGPS|In–Li symmetric cells, which experience significant volume changes in the In–Li anodes.<sup>[13,14]</sup> Based on these findings, the miniaturization of LGPS particles is anticipated to enhance the charge–discharge properties of thick composite electrodes.

In this study, we fabricated LCO-LGPS composite cathodes (400 μm thickness), which are 10 times thicker than typical cathodes used in laboratory-scale studies. This was achieved using WM-LGPS and hand-milled LGPS (HM-LGPS) prepared in an agate mortar. The cross sections of the resulting 400 μm-thick cathodes were observed *in situ* using a scanning electron microscope (SEM) with an energy-dispersive X-ray spectrometer specifically designed for the observation of ASSBs.<sup>[13,15,16]</sup> After charge and discharge cycles, the cracks formed in the composite using WM-LGPS self-closed, resulting in high-capacity retention. These findings provide new strategies for controlling the mechanical properties of ASSBs.

## 2. Results and Discussion

WM- and HM-LGPS utilized in this study were the same samples as those utilized in our previous study.<sup>[13,14]</sup> The ionic conductivities of WM- and HM-LGPS were 3.1 and 10 mS cm<sup>-1</sup>, respectively (Table S1, Supporting Information). In the particle size distribution, WM-LGPS and HM-LGPS exhibited the d<sub>50</sub> of 0.51 and 1.32 μm (Table S1, Supporting Information). SEM images also

indicated that huge particles in HM-LGPS were milled and disappeared, as shown in Figure S1, Supporting Information.

First, the charge–discharge properties of 40-LCO-LGPS|LGPS|In–Li cells were investigated using typical cells, commonly utilized in charge–discharge tests of ASSBs under pressing conditions, to clarify the contributions of HM- and WM-LGPS to the cathode and solid electrolyte layers under standard thickness conditions (Figure S2, Supporting Information). The fabricated cells were denoted as (thickness)-LCO-LGPS(HM/WM)|LGPS(HM/WM)|In–Li. There were no significant differences in the charge–discharge curves at C-rates up to 1C (1.17 mA cm<sup>-2</sup>). All capacities up to 1C were relatively close to the theoretical capacity of LCO (137 mAh g<sup>-1</sup> at 4.2 V vs. Li<sup>+</sup>/Li). It is reported that potential windows of sulfide solid electrolytes, including LGPS, are calculated to be quite narrow (<1 V).<sup>[17]</sup> However, it is also reported that experimentally observed potential windows are much larger than the calculated potential windows.<sup>[17]</sup> We also reported that Li<sub>10</sub>GeP<sub>2</sub>S<sub>12</sub> was hardly oxidized at the voltage range up to 5 V vs. Li<sup>+</sup>/Li in the cyclic voltammogram of Li|Li<sub>10</sub>GeP<sub>2</sub>S<sub>12</sub>|Au cell.<sup>[18]</sup> Additionally, we have confirmed that LCO-LGPS composite cathodes are charged and discharged without drastic electrochemical degradation,<sup>[11]</sup> and that capacity fading of LCO-Li<sub>10</sub>GeP<sub>2</sub>S<sub>12</sub>|Li<sub>10</sub>GeP<sub>2</sub>S<sub>12</sub>|In–Li is caused by an increase in the resistance at Li<sub>10</sub>GeP<sub>2</sub>S<sub>12</sub>/In–Li interfaces rather than LCO/Li<sub>10</sub>GeP<sub>2</sub>S<sub>12</sub> interfaces.<sup>[19]</sup> Furthermore, we have also reported that charge–discharge properties of LCO-Li<sub>10</sub>GeP<sub>2</sub>S<sub>12</sub> composites are affected by their microstructures, even 40 μm-thick cathodes without electrochemical deactivation.<sup>[11]</sup> From these points, LGPS is not electrochemically deactivated so much. The disagreement with the calculated potential windows is due to the difference between thermodynamics and kinetics. The calculated potential windows are based on thermodynamical stabilities. However, actual electrochemical stabilities are derived from both thermodynamic and kinetic ones. Even outside the calculated (=theoretical = thermodynamical) potential windows, solid electrolytes are not electrochemically deactivated so much as long as decomposition rates are slow ( $\approx$ not kinetically active so much). At a C-rate of 2C (2.35 mA cm<sup>-2</sup>), only the 40-LCO-LGPS(WM)|LGPS(WM)|In–Li cell showed a significantly lower overvoltage during discharge compared to the others. The capacities at 5C (5.87 mA cm<sup>-2</sup>) were higher when WM-LGPS was used as the solid electrolyte layer. We have previously reported that it is difficult to operate HM-LGPS in the solid electrolyte layer steadily at current densities between 2.0 and 2.5 mA cm<sup>-2</sup> in Li–In|LGPS|In–Li symmetric cells, owing to a drastic increase in overvoltage caused by the 2D expansion of cracks.<sup>[13]</sup> Contrastingly, WM-LGPS remains operable even at current densities  $>2.5$  mA cm<sup>-2</sup>. Therefore, the difference in the charge–discharge curve stems not from the cathode layers, but from the solid electrolyte layers. Thus, LCO in all 40 μm-thick cathodes was effectively utilized.

Next, 400 μm-thick cathodes were investigated using the same cells, as all 40 μm-thick cathodes had shown significant activity, as shown in Figure 1. The 400-LCO-LGPS(HM)|LGPS(HM)|In–Li cell exhibited a lower charge capacity during the first charge compared to the theoretical capacity of LCO, even at 0.05C (0.59 mA cm<sup>-2</sup>) (Figure 1a). Subsequently, the capacity decreased with each discharge. For the 400-LCO-LGPS(WM)|LGPS(HM)|In–Li cell (Figure 1b),

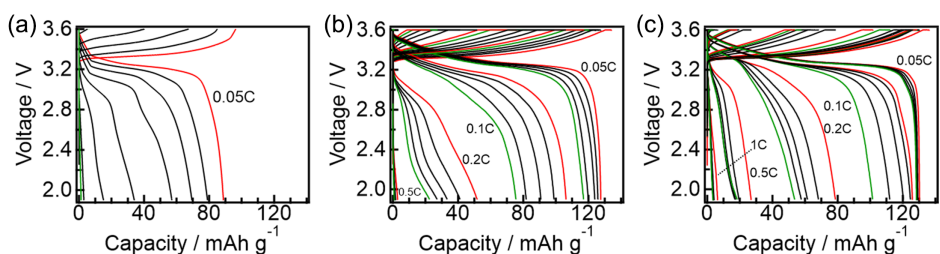


**Figure 1.** Charge-discharge curves at 1.9~3.6 V of a) 400-LCO-LGPS(HM)|LGPS(HM)|In-Li, b) 400-LCO-LGPS(WM)|LGPS(HM)|In-Li, and c) 400-LCO-LGPS(WM)|LGPS(WM)|In-Li. Charge and discharge were carried out with (CCCV) and CC modes, respectively. 0.05C corresponds to  $0.59 \text{ mA cm}^{-2}$  of the current density. Red and green curves mean initial and final cycles at each C-rate, respectively.

the charge capacity during the first cycle was approximately equal to the theoretical capacity. After the first charge, the capacity of 400-LCO-LGPS(WM)|LGPS(HM)|In-Li cell also decreased with each discharge, even though the rate of decrease was slower than that of the 400-LCO-LGPS(HM)|LGPS(HM)|In-Li cell. The decrease in capacity was drastically suppressed using WM-LGPS for the solid electrolyte layer at 0.05C (Figure 1c). However, the capacity still decreased during the first discharge in the 400-LCO-LGPS(WM)|LGPS(WM)|In-Li cell. In addition, when the C-rate exceeded 0.05C, the capacity decreased with each discharge, similar to other cells. Note that 0.05C for the 400  $\mu\text{m}$ -thick cathodes corresponds to the same current density ( $0.59 \text{ mA cm}^{-2}$ ) as 0.5C for the 40  $\mu\text{m}$ -thick cathodes. All 40  $\mu\text{m}$ -thick cathodes were steadily charged and discharged. Also in the Nyquist plots of LCO-LGPS|LGPS(WM)||In-Li cells before charge-discharge (Figure S3, Supporting Information), when the thickness was 40  $\mu\text{m}$ , there are no significant differences between HM- and WM-LGPS. In contrast, the semicircle component at the frequencies of  $10^4$ ~ $10^2$  Hz was drastically enlarged by using a 400  $\mu\text{m}$ -thick cathode comprising of HM-LGPS. The cell with a 400  $\mu\text{m}$ -thick cathode employing WM-LGPS also showed the larger semicircle component at the frequencies of  $10^2$ ~ $10^4$  Hz than those with the 40  $\mu\text{m}$ -thick cathodes. However, the difference of 400  $\mu\text{m}$ -thick cathode using WM-LGPS from the 40  $\mu\text{m}$ -thick ones was quite small, comparing to that of the 400  $\mu\text{m}$ -thick one using HM-LGPS. In LCO-LGPS|LGPS||In-Li cells, we have reported that semicircle components at the frequencies of  $10^2$ ~ $10^4$  Hz are derived from LCO-LGPS cathodes.<sup>[19,20]</sup> Therefore, the thickness and the microstructures affected the resistances of the charge-discharge reactions in the composite cathodes. These results of the EIS agree with the no obvious differences in charge-discharge properties between 40-LCO-LGPS(HM) and 40-LCO-LGPS(WM) (Figure S2a,b, Supporting Information), and the differences between 400-LCO-LGPS(HM) and 400-LCO-LGPS(WM) (Figure 1a,b). As the thickness of the cathodes is increased, areas of the LCO/LGPS interfaces are affected by the microstructures. Actually, LCO-LGPS(WM) exhibited a more uniform microstructure than LCO-LGPS(HM) in the cross-sectional SEM-EDX images (Figure 2). Thus, the resistances derived from LCO-LGPS largely differed between 400-LCO-LGPS(HM) and 400-LCO-LGPS(WM). Consequently, the decrease in capacity for the 400  $\mu\text{m}$ -thick cathodes can be intrinsically attributed to physical rather than electrochemical factors.

The 400-LCO-LGPS(HM)|LGPS(WM)|In-Li and 400-LCO-LGPS(WM)|LGPS(WM)|In-Li cells were observed *in situ* using

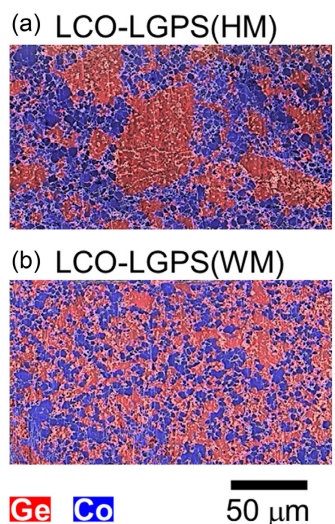


**Figure 2.** Cross-sectional SEM-EDX images of a) LCO-LGPS(HM) and b) LCO-LGPS(WM). The blue and red colors mean the existence of Co (LCO) and Ge (LGPS).

cross-sectional SEM-EDX to investigate the mechanical properties of the 400  $\mu\text{m}$ -thick cathodes. Herein, WM-LGPS was used as the solid electrolyte layer for both cell types, focusing on the differences derived from the cathode layers. Both cells exhibited relatively similar capacities ( $\approx 120$ – $130 \text{ mAh g}^{-1}$ ) compared to the theoretical capacity during the first charge, even in the press cells used for *in situ* SEM-EDX analysis (denoted as an *in situ* cell) (Figure S4, Supporting Information). However, LCO-LGPS(HM) showed a much larger decrease in capacity at the first discharge than LCO-LGPS(WM), even for *in situ* cells, as shown in the typical cells (Figure 1). At the first to fourth discharges, both cells showed steady charge-discharge cycles. These results also indicate a significant change during the first cycle. Figure 3 presents *in situ* cross-sectional SEM-EDX images of the LCO-LGPS(HM) cathode in a 400-LCO-LGPS(HM)|LGPS(WM)|In-Li cell. Cracks with widths ranging from several hundred nanometers to several micrometers were generated after the first charge and persisted even after the fourth discharge. The EDX mapping images revealed that the cracks tended to mainly appear at interfaces between LCO and other LCO particles. There was a small number of cracks at LCO/LGPS interfaces and in aggregated LGPS. Therefore, the decrease in capacity during the first discharge was mainly attributed to a reduction in active LCO, caused by the loss of

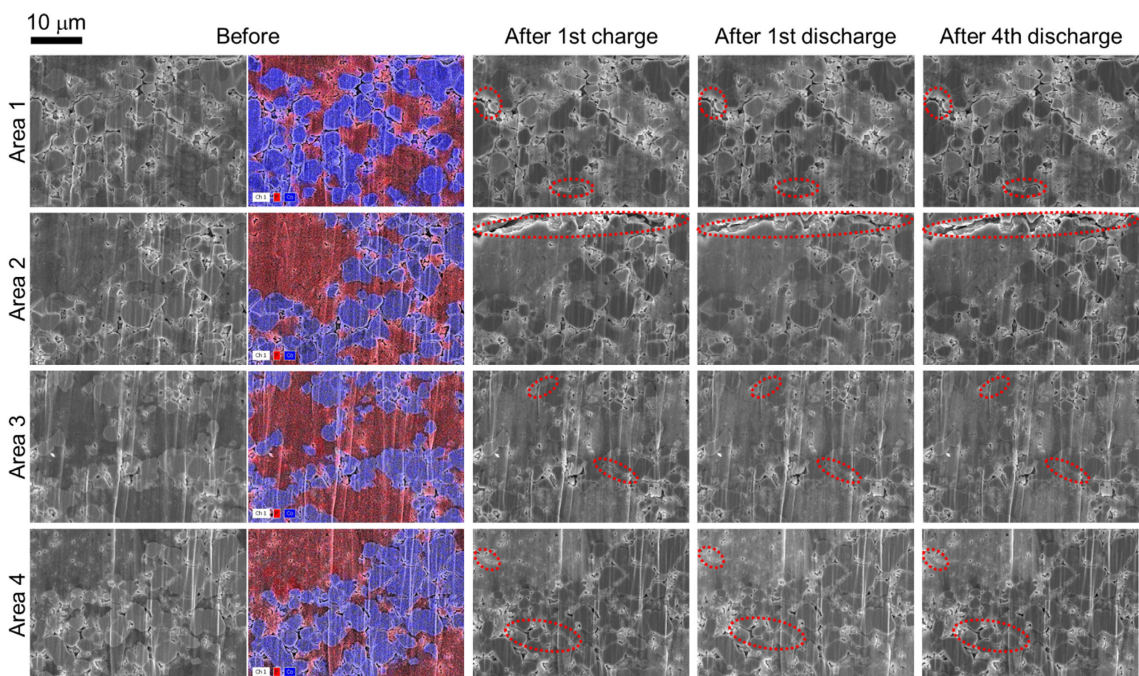


**Figure 3.** *In situ* cross-sectional SEM-EDX images of 400-LCO-LGPS(HM) composite cathode in 400-LCO-LGPS(HM)|LGPS(WM)||In–Li cell. The cracks generated during the first charge are surrounded by the red dashed circles. The blue and red colors in the EDX images mean the existence of Co (LCO) and P (LGPS). The charge-discharge curves are shown in Figure S4a, Supporting Information.

electron-conductive pathways. No new cracks were observed in areas where cracks had not formed after the first charge, even after the fourth discharge, leading to a minimal decrease in capacity after the first discharge.

The crack formation was also observed in the 400-LCO-LGPS(WM)|LGPS(WM)||In–Li cell after the first charge, as shown in Figure 4. The locations where the cracks generated tended to be mainly LCO/LCO interfaces, as seen also in the 400-LCO-LGPS(HM)|LGPS(WM)||In–Li. Of course, there was a small number of the cracks at LCO/LGPS interfaces and in aggregated LGPS. However, the cracks closed on their own after discharge regardless of the generated locations. Self-closing of the generated cracks enabled the LCO particles to continue functioning because the reaction sites and the electron/ion-conductive pathways were maintained. However, some cracks did not fully close and remained after the first discharge, leading to a small irreversible capacity loss during the first cycle. However, new cracks did not appear after the first charge, even after the fourth discharge. Then, the distribution of elements derived from LNO, LCO, and LGPS hardly changed after charge and discharge (Figure S5, Supporting Information). This is consistent with the high rate capability of 400-LCO-LGPS(WM) and stabilization role of LNO at interfaces between oxide active materials and sulfide solid electrolytes.<sup>[21]</sup> Also in the line scans crossing the LCO/LGPS interface after the first discharge and during the fourth discharge, O and S signals were separated from each other at the interface. This result also indicates that elemental compositions did not drastically change. However, the O signal during the fourth discharge seemed to invade the LGPS side a little, comparing with that after the first discharge. Therefore, there is a possibility that LGPS was oxidized a little during charge–discharge. We have

reported that  $\text{Li}_{10}\text{GeP}_2\text{S}_{12-x}\text{O}_x$  ( $x = 0.3$  and  $0.6$ ) show the ionic conductivities of  $10$  and  $8.4 \text{ mS cm}^{-1}$  at  $298 \text{ K}$ ,<sup>[22]</sup> which are relatively close to that of LGPS ( $14 \text{ mS cm}^{-1}$ ),<sup>[23]</sup> respectively. Consequently, even if the oxidation of LGPS really occurs, charge–discharge properties seem to hardly change. From these reasons, the  $400 \mu\text{m}$ -thick LCO-LGPS(WM) electrode could undergo steady charge–discharge cycles. Thus, using *in situ* SEM-EDX, the “self-closing” of the generated cracks, which is a significant phenomenon influencing the charge–discharge properties, could be observed. We have previously reported that WM-LGPS has a lower elastic modulus ( $15.0 \text{ GPa}$ ) and higher Meyer hardness ( $0.51 \text{ GPa}$ ) than HM-LGPS ( $21.7$  and  $0.41 \text{ GPa}$ ), respectively.<sup>[14]</sup> This means that WM-LGPS is more easily deformed elastically than HM-LGPS, while HM-LGPS is more easily deformed plastically than WM-LGPS. These differences in elastic and plastic deformability contribute to the presence or absence of self-closing of cracks, which in turn affect the charge–discharge properties. As mentioned earlier, LCO-LGPS(HM) exhibits an uneven microstructure (Figure 2). The uneven microstructure leads to localized stresses when the LCO particles expand during charging. The localized stresses are higher than the dispersed stresses due to focusing. Consequently, plastic rather than elastic deformation occurs, and plastic deformation is irreversible. Consequently, it is reasonable to conclude that the cracks generated in the  $400 \mu\text{m}$ -thick LCO-LGPS(HM) were not closed. In contrast, LCO-LGPS(WM) has a more uniform microstructure (Figure 2), which helps disperse stresses. This allows elastic deformation to dominate plastic deformation in the  $400 \mu\text{m}$ -thick LCO-LGPS(WM). Elastic deformation is reversible, which enables the generated cracks to close on their own in the  $400 \mu\text{m}$ -thick LCO-LGPS(WM). In this study, the effect of the self-closing is

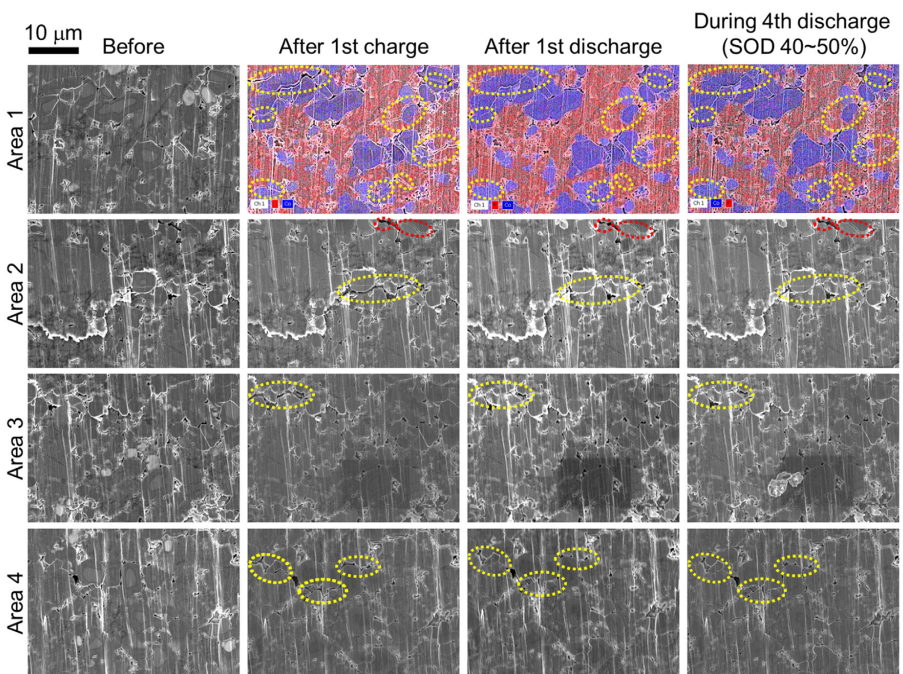


**Figure 4.** In situ cross-sectional SEM-EDX images of 400-LCO-LGPS(WM) composite cathode in 400-LCO-LGPS(WM)|LGPS(WM)|In-Li cell. The yellow dashed circles surround the cracks closing off by themselves during discharge after generating during the first charge. The red dashed circles are assigned to the cracks non-closing off completely. The blue and red colors in the EDX images mean existence of Co (LCO) and P (LGPS). The charge-discharge curves are shown in Figure S4b, Supporting Information.

discussed just in the case of the short-term charge–discharge cycling because of the limitation of the *in situ* observation system. Improving our *in situ* observation system would enable us to investigate the effects of the cracking and the self-closing on long-term charge–discharge cycling in the future.

When cracks are generated in active materials of batteries that use liquid electrolytes, the liquid can penetrate the cracks, appearing new interfaces between the active materials and the electrolytes. The new interfaces promote undesirable side reactions, such as decomposition of the electrolytes, reconstruction of surface atoms, formation of high-resistance species, and dissolution of transition metals in the active materials, resulting in capacity fading.<sup>[24–31]</sup> Therefore, the crack generation in batteries with liquid electrolytes should be suppressed for long cycle stabilities. In contrast, crack generation does not promote the undesirable side reactions in ASSBs because solid electrolytes cannot penetrate the cracks. Therefore, reactive interfaces and conductive pathways can be healed on their own through self-closing without increasing the number of undesirable side reactions. From this perspective, ASSBs possess more potential for cycle stability than LIBs as long as generated cracks self-close.

### 3. Conclusion

We have successfully controlled the microstructure of 400 μm-thick LCO-LGPS composites, which are ten times thicker than those typically fabricated at the laboratory scale, resulting in improved capacity and retention. *In situ* cross-sectional SEM-EDX imaging revealed that cracks generated during charging

closed off by themselves, during discharge in 400 μm-thick LCO-LGPS(WM), leading to high-capacity retention by maintaining contact between particles. This self-closing of the generated cracks was not observed in LCO-LGPS(HM), which showed low capacity-retention. The difference in self-closing behavior depends on the variations in the microstructures of the composites and the mechanical properties of LGPS. Elastic deformability, discussed with elastic moduli and yield stresses, is especially significant for reversible deformation of solid electrolytes. This finding of crack self-closing provides new strategies for improving the microstructure and mechanical properties of ASSBs.

## 4. Experimental Section

### Sample Preparation

The LGPS solid electrolytes utilized in this study were the same as those reported in our previous study.<sup>[13]</sup> Li<sub>2</sub>S (Mitsuwa Chemical; 99.9%), P<sub>2</sub>S<sub>5</sub> (Sigma-Aldrich; 99%), and GeS<sub>2</sub> (Kojundo Chemical; 99.99%) were utilized as starting materials. The starting materials were ground in an agate mortar for 15 min. The mixture was milled with ZrO<sub>2</sub> balls (10 mm in diameter) in a ZrO<sub>2</sub> pot for 40 h at 380 rpm using a planetary mill (Fritsch; Pulverisette 7). The ball-milled precursor was pelletized and subsequently sealed in a quartz ampoule under vacuum. The pellets in the ampoule were heated in an electric furnace at 823 K for 8 h, with the temperature increased at a rate of 5 K min<sup>-1</sup>. After heating, the pellets were ground in an agate mortar for 5 min to obtain powdered LGPS. This powdered LGPS was further processed to produce HM- and WM-LGPS.<sup>[13]</sup> HM-LGPS was obtained by additional grinding in the agate mortar for 25 min, resulting in a total grinding time of 30 min. For the WM-LGPS, the powdered LGPS was milled using the planetary mill with a ZrO<sub>2</sub> pot containing ZrO<sub>2</sub>

balls (5–10 mm in diameter) and anhydrous heptane (Wako Pure Chemicals; 99.0%) at 300 rpm for 80 min. The ball-milled samples were then dried for 12 h under vacuum.

The LCO-LGPS composite cathodes were fabricated according to a previous report.<sup>[19]</sup> LCO (coated with amorphous LiNbO<sub>3</sub>) and the obtained LGPS were mixed with agate balls (3 mm in diameter) in a glass vial for 20 min at 140 rpm using a pot mill rotator (Nitto; ANZ-10S). The LCO to LGPS ratio was 7:3 by weight, corresponding to a 5:5 ratio by volume.

ASSBs were fabricated using LCO-LGPS composites as cathodes, LGPS as solid electrolyte layers, and In–Li as anodes. LGPS (80 mg) for the solid electrolyte layers was first pelletized at 110 MPa for 1 min. LCO-LGPS composites and Al meshes for current collectors were added on the top faces of the pelletized LGPS and subsequently pressed at 550 MPa for 1 min. In and Li foils were placed on the faces opposite the LCO-LGPS composite layers, with Cu meshes for the current collectors placed on the In and Li foils. Then, 220 MPa of pressure was applied to the pellets for 3 s, resulting in Al|LCO-LGPS|LGPS|In–Li|Cu cells. For *in situ* SEM-EDX observations, the obtained ASSB pellets were cut with a slicer (JASCO; Multi-Angle Slicer HW-1) to expose their cross sections, which were then flattened for 2 h using a focused Ar-ion beam (Hitachi High-Tech; IM4000) with an acceleration voltage of 6 kV during cooling at 183 K.

### Usual Charge–Discharge Measurements

The charge–discharge properties of the obtained ASSBs were first investigated using typical cells, which were commonly used for charge–discharge tests of pelletized ASSBs under pressing conditions. Charge and discharge were carried out at 1.9~3.6 V vs. In–Li anodes ( $\approx$ 2.5~4.2 V vs. Li<sup>+</sup>/Li) using constant-current + constant-voltage (CCCV) and constant-current (CC) modes, respectively. The C-rates in CC mode were 0.5~5C and 0.05~1C for 40 and 400  $\mu$ m-thick cathodes, respectively, implying that 0.5C for 40  $\mu$ m-thick cathodes correspond to the same current density (0.59 mA cm<sup>-2</sup>) as 0.05C for 400  $\mu$ m-thick cathodes.

### In Situ Cross-Sectional SEM-EDX Observations

A field-emission SEM (Hitachi High-Tech; Regulus 8230) equipped with an energy-dispersive X-ray spectroscope (EDX, Bruker; QUANTAX FlatQUAD, Figure S6, Supporting Information) was utilized to observe *in situ* cross sections of ASSBs during charge–discharge tests, as described in our previous reports.<sup>[13,15,16]</sup> The ASSB pellets with flattened cross sections were placed into cells designed specifically for *in situ* observation with the SEM-EDX system (denoted as *in situ* cell). The *in situ* cell was electrically connected to a potentiostat/galvanostat (Biologic; SP-50) via terminals inside and outside the SEM body. Charge and discharge were carried out within the SEM chamber at 1.9~3.6 V vs. In–Li using CCCV and CC modes, respectively, with a C-rate of 0.05C in CC mode. After charging and discharging, cross-sectional images were observed and captured *in situ* using SEM-EDX. In the case of composite electrodes in pelletized ASSBs, the *in situ* observation system is limited to tests during short-term (5~10th) cycling due to the physical structure of the *in situ* cell.<sup>[15]</sup> However, we have confirmed that the system can be applied to *in situ* observation as long as the short-term cycling.

### Acknowledgements

This study was partially supported by a Grant-in-Aid for Scientific Research on Innovative Areas (grant no. 19H05793) from the Japan Society for the Promotion of Science (JSPS), and the

GteX Program (grant no. JPMJGX23S5) provided by the Japan Science and Technology Agency (JST). The authors gratefully thank Mr. B.Y. Kang for assistance with the electrochemical impedance spectroscopy (EIS) measurements.

### Conflict of Interest

The authors declare no conflict of interest.

### Data Availability Statement

Research data are not shared.

**Keywords:** all-solid-state batteries • crack self-closing • *in situ* scanning electron microscopy with energy-dispersive X-ray spectroscopy • microstructures • thick composites

- [1] Y. Kato, K. Kawamoto, R. Kanno, M. Hirayama, *Electrochemistry* **2012**, *80*, 749.
- [2] F. Strauss, T. Bartsch, L. de Biasi, A.-Y. Kim, J. Janek, P. Hartmann, T. Brezesinski, *ACS Energy Lett.* **2018**, *3*, 992.
- [3] A. Bielefeld, D. A. Weber, J. Janek, *J. Phys. Chem. C* **2019**, *123*, 1626.
- [4] D. Park, K. Kim, H.-S. Kim, H. Seo, H. S. Lee, H. Choi, J.-H. Kim, *Electron. Mater. Lett.* **2020**, *16*, 376.
- [5] J. K. Eckhardt, S. Burkhardt, J. Zahnow, M. T. Elm, J. Janek, P. J. Klar, C. Heiliger, *J. Electrochem. Soc.* **2021**, *168*, 090516.
- [6] A. Verma, H. Wakakami, H. Wada, A. Hirowatari, N. Ikeda, Y. Mizuno, T. Kotaka, K. Aotani, Y. Tabuchi, P. P. Mukherjee, *Cell Rep. Phys. Sci.* **2021**, *2*, 100301.
- [7] J. Zhang, Z. Chen, Q. Ai, T. Terlier, F. Hao, Y. Liang, H. Guo, J. Lou, Y. Yao, *Joule* **2021**, *5*, 1845.
- [8] D. K. Singh, A. Henss, B. Mogwitz, A. Gautam, J. Horn, T. Krauskopf, S. Burkhardt, J. Sann, F. H. Richter, J. Janek, *Cell Rep. Phys. Sci.* **2022**, *3*, 101043.
- [9] Z. Ding, Y. Tang, T. Ortmann, J. K. Eckhardt, Y. Dai, M. Rohrke, G. Melinte, C. Heiliger, J. Janek, C. Kübel, *Adv. Energy Mater.* **2023**, *13*, 2302322.
- [10] D. K. Singh, T. Fuchs, C. Krempaszky, B. Mogwitz, S. Burkhardt, F. H. Richter, J. Janek, *Adv. Funct. Mater.* **2023**, *33*, 2211067.
- [11] Y. Yamada, K. Watanabe, H.-S. Kim, K. Suzuki, S. Hori, R. Kanno, M. Hirayama, *Batteries Supercaps* **2023**, *6*, e202300261.
- [12] P. Minnmann, J. Schubert, S. Kremer, R. Rekers, S. Burkhardt, R. Ruess, A. Bielefeld, F. H. Richter, J. Janek, *J. Electrochem. Soc.* **2024**, *171*, 060514.
- [13] H.-S. Kim, K. Watanabe, N. Matsui, K. Suzuki, R. Kanno, M. Hirayama, *Batteries Supercaps* **2023**, *6*, e202300306.
- [14] H. Kim, K. Hikima, K. Watanabe, N. Matsui, K. Suzuki, S. Obokata, H. Muto, A. Matsuda, R. Kanno, M. Hirayama, *Mater. Trans.* **2024**, *65*, 861.
- [15] T. Noda, H. Kim, K. Watanabe, K. Suzuki, N. Matsui, R. Kanno, M. Hirayama, *J. Ceram. Soc. Jpn.* **2023**, *131*, 651.
- [16] P. Jiang, H. Zhou, S. Song, K. Suzuki, K. Watanabe, Y. Yamaguchi, N. Matsui, S. Hori, R. Kanno, M. Hirayama, *Commun. Mater.* **2024**, *5*, 105.
- [17] K. J. Kim, M. Balaish, M. Wadaguchi, L. Kong, J. L. M. Rupp, *Adv. Energy Mater.* **2021**, *11*, 2002689.
- [18] N. Kamaya, K. Homma, Y. Yamakawa, M. Hirayama, R. Kanno, M. Yonemura, T. Kamiyama, Y. Kato, S. Hama, K. Kawamoto, A. Mitsui, *Nat. Mater.* **2011**, *10*, 682.
- [19] W. J. Li, M. Hirayama, K. Suzuki, R. Kanno, *Solid State Ion.* **2016**, *285*, 136.
- [20] S. Hori, R. Kanno, X. Sun, S. Song, M. Hirayama, B. Hauck, M. Dippon, S. Dierickx, E. Ivers-Tiffée, *J. Power Sources* **2023**, *556*, 232450.
- [21] N. Ohta, K. Takada, I. Sakaguchi, L. Zhang, R. Ma, K. Fukuda, M. Osada, T. Sasaki, *Electrochim. Commun.* **2007**, *9*, 1486.
- [22] Y. Sun, K. Suzuki, K. Hara, S. Hori, T. Yano, M. Hara, M. Hirayama, R. Kanno, *J. Power Sources* **2016**, *324*, 798.
- [23] O. Kwon, M. Hirayama, K. Suzuki, Y. Kato, T. Saito, M. Yonemura, T. Kamiyama, R. Kanno, *J. Mater. Chem. A* **2015**, *3*, 438.
- [24] S. Watanabe, M. Kinoshita, T. Hosokawa, K. Morigaki, K. Nakura, *J. Power Sources* **2014**, *258*, 210.

- [25] H. Liu, M. Wolfman, K. Karki, Y.-S. Yu, E. A. Stach, J. Cabana, K. W. Chapman, P. J. Chupas, *Nano Lett.* **2017**, *17*, 3452.
- [26] H.-H. Sun, A. Manthiram, *Chem. Mater.* **2017**, *29*, 8486.
- [27] H.-H. Ryu, K.-J. Park, C. S. Yoon, Y.-K. Sun, *Chem. Mater.* **2018**, *30*, 1155.
- [28] Z. Xu, M. M. Rahman, L. Mu, Y. Liu, F. Lin, *J. Mater. Chem. A* **2018**, *6*, 21859.
- [29] W. Wang, Q. Yang, K. Qian, B. Li, *J. Energy Chem.* **2020**, *47*, 72.
- [30] H. Kaneda, Y. Furuichi, A. Ikezawa, H. Arai, *ACS Appl. Mater. Interfaces* **2022**, *14*, 52766.
- [31] S. P. Kühn, K. Edström, M. Winter, I. Čekic-Laskovic, *Adv. Mater. Interfaces* **2022**, *9*, 2102078.

Manuscript received: February 19, 2025  
Revised manuscript received: April 16, 2025  
Version of record online: April 21, 2025